



Fatigue damage evolution and lifetime prediction of welded joints with the consideration of residual stresses and porosity



Fei Shen^a, Bo Zhao^a, Lin Li^b, Chee Kai Chua^a, Kun Zhou^{a,*}

^aSchool of Mechanical and Aerospace Engineering, Nanyang Technological University, 639798 Singapore, Singapore

^bLaser Processing Research Centre, School of Mechanical, Aerospace and Civil Engineering, The University of Manchester, Manchester, UK

ARTICLE INFO

Article history:

Received 13 March 2017

Received in revised form 8 June 2017

Accepted 8 June 2017

Available online 10 June 2017

Keywords:

Fatigue damage evolution

Lifetime prediction

Welded joints

Residual stresses

Porosity

ABSTRACT

This work investigates the fatigue damage evolution of butt welded joints under cyclic loading through a continuum damage mechanics approach. A coupled thermal-mechanical analysis is conducted to evaluate the residual stresses induced by welding processes, which are used as the initial state in the fatigue damage analysis. An elasto-plastic fatigue damage model that takes into account the porosity-induced stress concentration in the weld zones of joints is developed to study their damage evolution. The fatigue lifetimes of these joints with different pore conditions are predicted and show consistency with the experimental results. The residual stress level is found to decrease due to the combined effects of the plastic deformation and fatigue damage.

© 2017 Elsevier Ltd. All rights reserved.

1. Introduction

Fatigue is the dominant failure mode of welded joints under cyclic loading [1,2]. Extensive tests of the fatigue performance of welded joints have been conducted over the past decades. Several standards such as Eurocode 9 [3] and International Institute of Welding recommendations [4] have been published to provide guidelines for fatigue assessment and design of these joints. The fatigue strength is influenced not only by the material fatigue property and cyclic loading conditions but also by the welding process-induced changes in joints such as the residual stresses and welding defects. Due to the intense concentration of heating and subsequent cooling, residual stresses are inevitably formed in the fusion zone (FZ) and heat-affected zone (HAZ). These residual stresses are superimposed on the cyclic loading, leading to a significant increase in the maximum stress and mean stress levels and thus reducing the fatigue lifetime. Moreover, the weld characteristics such as increased flank angle, excess weld metal, angular distortion, misalignment and pores result in the stress concentrations and detriment the fatigue performance.

Pores inside the welded joints are mainly attributed to the trapping of shielding gases, hydrogen, and process vapors. In the presence of the pores, the effective carrying area is reduced, which increases the average stress level in the weld zone. Pores also cause

the stress concentration and provide the potential sites for the early cracks initiation [5,6]. Therefore, how to control the porosity is a critical issue in the welding process as well as the additive manufacturing [7,8]. With the development of the non-destructive testing (NDT) methods, the pore conditions such as the maximum diameter, average size and number of pores can be evaluated from the scanning results [9–11]. However, few researches were conducted to consider the effect of porosity on the fatigue lifetimes of these joints, which can be attributed to two reasons: (a) the characteristic of porosity is difficult to control during welding processes; (b) it is a challenge to distinguish the effect of porosity from other factors in the fatigue testing.

Stress-based approach [12] and fracture mechanics approach [13] are two main methods used to assess the fatigue lifetimes of welded joints [14]. The former approach is based on *S-N* curves that correlate the number of cycles *N* that causes failure to the applied cyclic stress range *S*. The stress range can be expressed in terms of nominal stress, hot-spot stress or local notch stress. The *S-N* curves are derived from many fatigue experiments with particular weld details, which include the influences of the residual stresses and porosity. The fracture mechanics approach focuses on the propagation behaviour of cracks originating from material manufacturing or welding processes or the crack initiation under service loads. Welding defects detected by the use of NDT methods are categorized as initial cracks with elliptical shapes [13]. However, it ignores the crack initiation period, leading to serious underestimation of the fatigue lifetime particularly in the high-cycle

* Corresponding author.

E-mail address: kzhou@ntu.edu.sg (K. Zhou).

fatigue regime. Furthermore, it is limited by the distribution of pores and their possible interactions in joints. Although they are widely used to assess the fatigue lifetimes, both approaches cannot take into account the evolution of fatigue damage and its influence on the material properties.

Continuum damage mechanics (CDM) approach has been introduced to the fatigue damage analysis of welded joints under cyclic loading. A damage variable defined as a measurement of micro-cracks and micro-voids in the material is incorporated into the fatigue damage model. It deals with the mechanical behaviour of a deteriorated material at the macroscopic scale and evaluates the progressive damage based on the evolution law derived from thermodynamics [15,16]. Do et al. [17] used a CDM approach to investigate the effect of residual stresses in butt welds on their fatigue lifetimes. It was reported that the fatigue crack initiation period consumed the majority of total fatigue lifetime in the high-cycle fatigue regime. He et al. [18] developed a fatigue model based on the change of natural frequency of welded joints to describe their damage evolution. It captured the elasto-plastic deformation and residual stress relaxation. However, the porosity is not considered in the aforementioned investigations.

This study investigates the fatigue damage evolution of welded joints in the presence of residual stresses and porosity. A couple thermal-mechanical analysis is conducted to obtain the distribution of residual stresses in joints. A fatigue damage model is developed to evaluate the fatigue damage evolution of these joints, in which the stress concentration induced by pores is considered to be relevant with the maximum diameter of pores. Their fatigue lifetimes with different pore conditions are predicted regarding the obtained residual stresses as the initial state of these calculations and show consistency with the experimental results. It is found that the residual stresses gradually relax with the increasing number of loading cycles due to the combined effects of the stress redistribution and fatigue damage.

2. Fatigue damage model development

2.1. Damage-coupled elasto-plastic constitutive model

Fatigue is a process of the nucleation of micro-voids and micro-cracks and subsequent coalescence and propagation occurring under cyclic loading. In the framework of CDM, the effect of these defects on the mechanical behaviour of materials is analyzed through a macroscopic internal damage variable in the representative volume element (RVE). The damage variable D for the isotropic damage case is defined as the ratio of the area of defects S_D to the total section area S , as shown in Fig. 1.

$$D = \frac{S_D}{S}. \quad (1)$$

The introduction of the damage variable leads to the effective stress expressed as

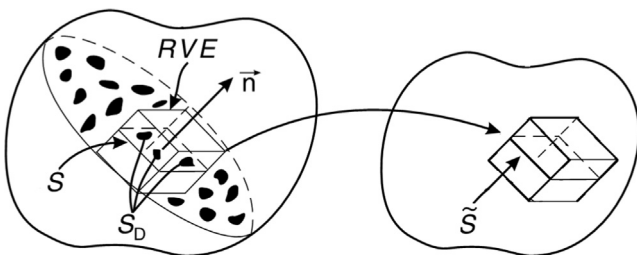


Fig. 1. Schematic view of RVE [19].

$$\tilde{\sigma} = \frac{\sigma}{1 - D}, \quad (2)$$

where σ is the Cauchy stress tensor. This effective stress is considered in a fictitious state where the material is totally undamaged (i.e., the damage in the real state has been removed) and the effective section area is reduced to $\tilde{S} = S(1 - D)$, as shown in Fig. 1.

The elasto-plastic constitutive model is used to evaluate the stresses and strains since the plastic deformation may occur in the weld zone due to the presence of tensile residual stresses. With the consideration of fatigue damage, the damage variable is integrated into the Chaboche plasticity model [20,21] by using the effective stress in lieu of the Cauchy stress in the model, which is based on the hypothesis of strain equivalence [19]. The decomposition of total strain under the small strain assumption is expressed by

$$\epsilon = \epsilon^e + \epsilon^p, \quad (3)$$

where the tensors ϵ^e and ϵ^p are the elastic strain and plastic strain, respectively. The elastic law is expressed by

$$\sigma = (1 - D)\mathbf{C}^e : \epsilon^e, \quad (4)$$

where \mathbf{C}^e is the fourth-order tensor of elastic moduli that can be described by Young's modulus E and Poisson's ratio ν . The yield function and plastic flow are respectively expressed by

$$f = \|\mathbf{s}/(1 - D) - \alpha\| - \sigma_f$$

$$= \sqrt{\frac{3}{2}(\mathbf{s}/(1 - D) - \alpha) : (\mathbf{s}/(1 - D) - \alpha) - \sigma_f}, \quad (5)$$

$$\dot{\epsilon}^p = \lambda \frac{\partial f}{\partial \sigma} = \frac{3}{2} \frac{\lambda}{1 - D} \frac{\mathbf{s}/(1 - D) - \alpha}{\|\mathbf{s}/(1 - D) - \alpha\|}, \quad (6)$$

$$\dot{p} = \sqrt{\frac{2}{3} \dot{\epsilon}^p : \dot{\epsilon}^p} = \frac{\lambda}{1 - D}, \quad (7)$$

where \mathbf{s} and α represent the deviatoric parts of Cauchy stress and back stress, respectively. The term λ is the plastic multiplier and \dot{p} is the accumulated plastic strain rate. In this study the isotropic hardening law is ignored and thus the yield stress σ_f is assumed to remain unchanged. The kinematic hardening law is expressed by

$$\alpha = \sum_{k=1}^K \alpha_k, \quad (8)$$

$$\dot{\alpha}_k = (1 - D) \left(\frac{2}{3} C_k \dot{\epsilon}^p - \gamma_k \alpha_k \dot{p} \right), \quad (9)$$

where K is the number of the back stress components. Parameters C_k and γ_k are material constants obtained from experiments.

2.2. Damage evolution model development

In the regime of high-cycle fatigue, the cyclic stress determines the fatigue lifetime of the unwelded material. The evolution law of fatigue damage in the uniaxial stress case can be expressed by [22]

$$\frac{dD}{dN} = a \left(\frac{\sigma_a}{(1 - b\sigma_m)(1 - D)} \right)^\beta, \quad (10)$$

where σ_a and σ_m are the stress amplitude and the mean stress, respectively. The material parameters a , b and β are determined from the fatigue testing of the unwelded material. Under the multi-axial stress state, the above evolution law is rewritten as [23]

$$\frac{dD}{dN} = a \left(\frac{A_{II}}{(1 - 3b\sigma_{H,mean})(1 - D)} \right)^\beta, \quad (11)$$

$$A_{II} = \frac{1}{2} \left[\frac{3}{2} (S_{ij,max} - S_{ij,min})(S_{ij,max} - S_{ij,min}) \right]^{1/2}, \quad (12)$$

$$\sigma_{H,mean} = \frac{1}{6} (\sigma_{kk,max} + \sigma_{kk,min}), \quad (13)$$

in which the amplitude of octahedral shear stress A_{II} and the mean hydrostatic stress $\sigma_{H,mean}$ are used instead of the stress amplitude and mean stress respectively. This model can provide reasonable predictions of the fatigue lifetimes for notched specimens made of aluminium alloy [24]. Actually, the term $A_{II}/(1-D)$ can be regarded as the effective stress amplitude, representing the average effect of damage on the reduction of load-resisting area. However, the stress concentration effect of pores is not considered in this model.

In the numerous investigations [25–28], the pores are regarded as high risks for the initiation and propagation of cracks. The finite element method is widely used to calculate the stress field in the bulk materials containing pores, which provides a simple approach to investigate the pore-induced stress concentration effect. It was also used to evaluate the scatter of fatigue lifetimes induced by pores or flaws, in which the properties of the elements randomly selected to represent the pores are reduced to 50% of virgin material properties [29]. With the development of X-ray scanning technology, the status of pores can be inspected and employed in the simulation. However, a challenge still remains on the aspects such as the modelling and simulation efficiency. Therefore, the distribution of pores is not considered in this study.

It was reported that the fatigue crack initiated around the pore with maximum diameter in welded joints under different pore conditions [30]. In the present study, the maximum pore diameter is used to describe the stress concentration effect on the fatigue lifetime. As the pore diameter increases, the stress concentration factor increases and thus reduce the fatigue lifetime [31]. Therefore, the damage evolution model for welded joints is proposed as

$$\frac{dD}{dN} = a \left(\frac{A_{II}(1 + d_{max}^c)}{(1 - 3b\sigma_{H,mean})(1 - D)} \right)^\beta, \quad (14)$$

where d_{max} is the maximum diameter of the pores and c is a material parameter that is determined through the fatigue testing of welded joints. The term $A_{II}(1 + d_{max}^c)$ represents the effect of stress concentration induced by pores. After the welding processes, the variable d_{max} can be obtained through NDT. It is noted that the possible growth of pores under the cyclic loading is ignored during the evaluation of fatigue damage evolution.

3. Fatigue lifetime prediction of welded joints

A recent experimental study on the aluminium alloy welded joints showed that the porosity significantly affects their fatigue strength [30]. The base material of the sheets with 8 mm thickness was an Al-Zn-Mg alloy (A7N01S) under T5 heat treatment. This material has similar chemical composition with AA7005 aluminium alloy and its mechanical properties are listed in Table 1. The joints were welded using gas metal arc welding (GMAW) processes with 1.2 mm diameter ER5356 filler wire, of which the material properties are also shown in Table 1. The process param-

eters of the three passes are listed in Table 2. The processes under five environment humidity levels were conducted to obtain different pore conditions as shown in Table 3. Fatigue samples were machined from the welded sheets in the direction perpendicular to the welding direction, as shown in Fig. 2. Weld reinforcements were removed to meet the standard requirement of fatigue testing. The stress ratio of fatigue loading was $R = 0$ and the test frequency was in the range of 90–110 Hz.

3.1. Residual stress analysis

The welding processes involve complex phenomena arising from the interactions between the heat transfer, metallurgical transformation and mechanical behaviour. Residual stresses are induced in the heating and subsequent cooling processes, which is critical to the fatigue assessment of welded joints. However, the results of the residual stress field are not available in the literature [30]. Therefore, a numerical residual stress analysis is needed.

A coupled thermal-mechanical analysis is used to evaluate the residual stresses in the welded joints. The heat source is described by two ellipsoid distributions in the GOLDAK model [33,34]

$$q(x, y, z, t) = \frac{6\sqrt{3}f_f\eta Q}{lm_f n\pi\sqrt{\pi}} \exp\left(-\frac{3x^2}{l^2} - \frac{3(y-vt)^2}{m_f^2} - \frac{3z^2}{n^2}\right), \quad (15)$$

$$q(x, y, z, t) = \frac{6\sqrt{3}f_r\eta Q}{lm_r n\pi\sqrt{\pi}} \exp\left(-\frac{3x^2}{l^2} - \frac{3(y-vt)^2}{m_r^2} - \frac{3z^2}{n^2}\right), \quad (16)$$

where Q is the heat power, η the arc efficiency, f_f and f_r the heat input proportions in the front and rear regions, respectively, $f_f + f_r = 2$. The parameters l , m_f , m_r and n are set as 6.0, 7.0, 9.0 and 4.5 mm, respectively [35]. The parameters η , f_f and f_r are assumed to be 0.5, 1.4 and 0.6, respectively [36].

The element kill and rebirth method is employed to model the addition of filler material during the three passes [37–39]. All the elements in the weld zone are initially inactive before the welding process. For each pass, the elements in the pass are activated firstly and the welding processes are simulated by moving the heat source on these elements. A short cooling time between these passes is applied in the simulation. The model gradually cools down to the room temperature after the third welding pass. The thermal radiation and convection boundaries are set corresponding for each pass due to the model change.

Temperature-dependent physical constants and mechanical properties are shown in Fig. 3. A perfect yield model is used which ignores the plastic hardening. It is reported that the simulation results obtained by using the perfect yield model is nearly identical to those obtained by using the model considering the strain hardening [35]. The filler material ER5356 is different from the base material. It will be more reasonable to consider this difference if the thermal and mechanical properties of both materials are implemented in the simulation of the residual stress. However, the temperature-dependent properties of the material ER5356 are not available in the literature. Therefore, the difference between the material properties of the base material and filler material is not considered in this study. The phase transformation

Table 1
Material mechanical properties [30,32].

Material	Tensile strength (MPa)	Yield stress (MPa)	Elongation (%)
Al-Zn-Mg alloy	393	327	15.5
ER5356	265	120	26

Table 2
Welding process parameters [30].

Pass	Peak current (A)	Voltage (V)	Speed (mm/min)
1	170–189	20.3–22.7	600–656
2	174–195	21.4–22.9	636–656
3	176–191	22.1–23.2	500–525

Table 3
Pore conditions under different humidity levels [30].

Humidity (%)	Mean size (mm)	Maximum diameter (mm)	Maximum area (mm ²)	Total area (mm ²)
50	0.00005	0.06	0.0017	0.002
60	0.0012	0.11	0.0078	0.14
70	0.005	0.72	0.3344	0.96
80	0.0018	0.29	0.0484	0.35
90	0.0004	0.16	0.0188	0.21

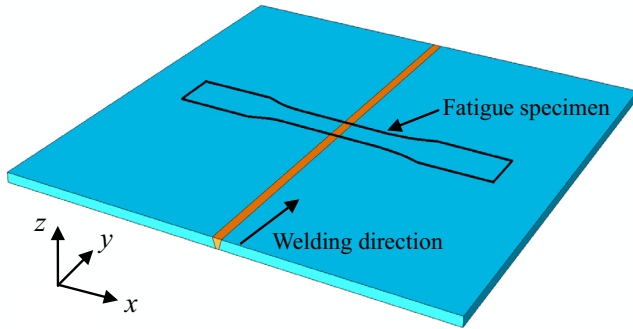
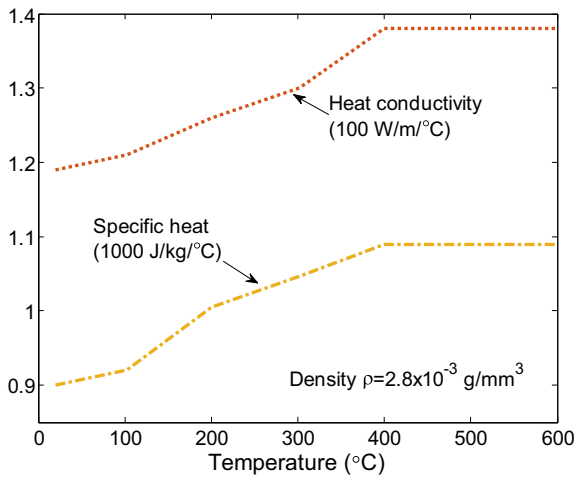
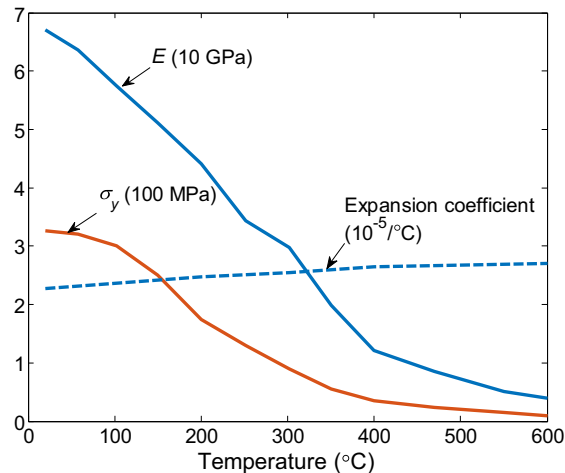


Fig. 2. Schematic view of the welding configuration and fatigue specimen.



(a)



(b)

Fig. 3. Temperature-dependent physical constants (a) and mechanical properties (b).

is also not taken into account. The welding direction is along the y-direction, as shown in Fig. 2. The displacements of two side surfaces are constrained and the displacement along the z-direction of the bottom surface is fixed to eliminate the distortion induced by the welding processes.

The residual stresses in x- and y-direction along the path on the top surface are depicted in Fig. 4. The longitudinal stress σ_y with the maximum value of around 360 MPa is larger than the transverse stress σ_x . Both residual stresses decrease from the tensile state in the weld zone to the compression state and then approach to zero as the position is away from the welding centreline. Fig. 5 shows the distribution of σ_x on the gauge part of the middle cross section in joints. The maximum value occurs beneath the top surface. The similar results were reported in the literature [40]. Because the cyclic loading is applied in the x-direction, the residual stress along this direction is critical to the prediction of fatigue damage and lifetime. The multiaxial residual stress field obtained in this analysis will be imported into the subsequent fatigue damage analysis.

3.2. Determination of material parameters

The material parameters of the Al-Zn-Mg alloy in the elastoplastic constitutive model are calibrated using monotonic or cyclic stress-strain data. The integration of Eq. (9) under the uniaxial loading leads to the stress-strain curve expressed as

$$\sigma = \sum_{k=1}^K \frac{C_k}{\gamma_k} (1 - e^{-\gamma_k \epsilon^p}) + \sigma_y. \quad (17)$$

The least square fitting is employed to obtain the parameters C_k and γ_k , as shown in Fig. 6. In this study, two groups of back stresses are used ($K = 2$). The material parameters of the constitutive model are determined as listed in Table 4.

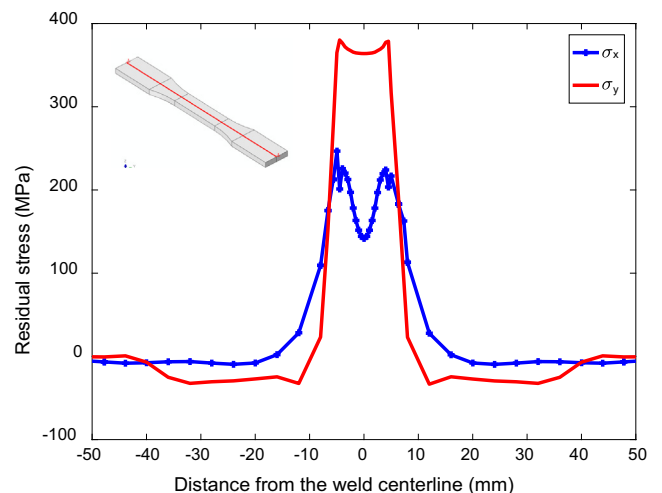


Fig. 4. Distributions of residual stresses σ_x and σ_y along the path.

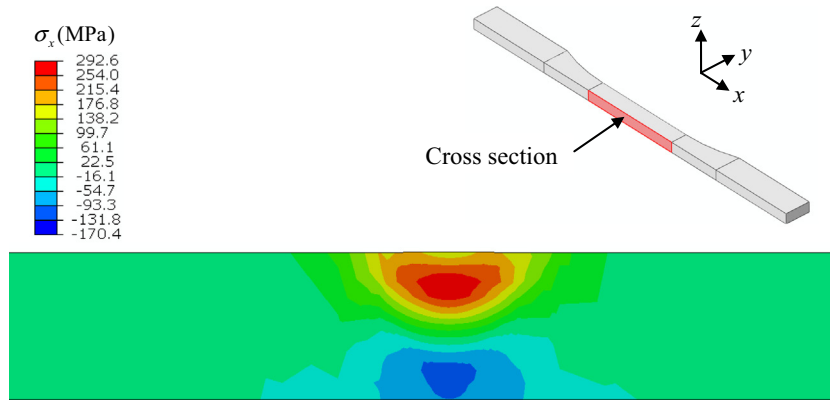


Fig. 5. Contour of residual stress σ_x on the cross section.

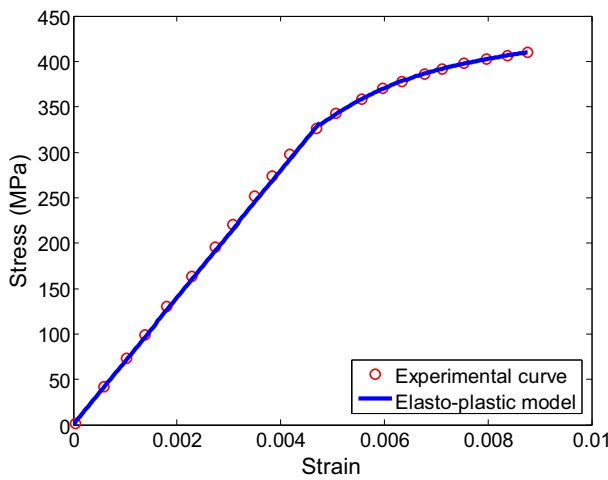


Fig. 6. Stress–strain curve for the Al-Zn-Mg alloy.

For the damage evolution model, the integration of Eq. (11) from $D = 0$ to $D = 1$ under the uniaxial loading condition results in the fatigue lifetime-stress curve

$$N = \frac{1}{a(1 + \beta)} \left(\frac{\sigma_a}{1 - b\sigma_m} \right)^{-\beta} \quad (18)$$

The parameters a , b and β are determined through fatigue testing of the unwelded specimens under different stress ratios or mean stresses [41]. The integration of Eq. (14) for the welded specimens gives

$$N = \frac{1}{a(1 + \beta)} \left(\frac{\sigma_a(1 + d^c)}{1 - b\sigma_m} \right)^{-\beta} \quad (19)$$

The parameter c is needed to determine through the experimental data of welded specimens. In this study, the testing data with fatigue lifetimes around 1×10^6 cycles under five humidity conditions are used to determine this parameter [30]. However, it is impossible to obtain the material parameter c by directly using Eq. (19) that only considers the effect of porosity because the fatigue testing includes the combined effects of the residual stresses and porosity. The trial and error method is used to identify this parameter, as the

fatigue lifetimes predicted by the numerical approach proposed in the next subsection agree with the testing results (fatigue lifetimes around 1×10^6 cycles under five humidity conditions). The material parameters of the damage evolution model are listed in Table 5.

3.3. Fatigue damage analysis

The obtained residual stress field is used as the initial condition of the fatigue damage analysis. As shown in Fig. 7, the weld zone including the FZ and HAZ is in the middle part of the specimen. The length of the weld zone in the x -direction can be set as 20 mm based on the residual stress results in Fig. 4. It is noted that the damage-coupled constitutive model used here is different from that in the residual stress analysis. Since the pores induced by welding processes only exist in the weld zone, the evolution of fatigue damage in this zone is calculated by Eq. (14). The base material can be regarded as non-porous media and its damage evolution is evaluated by using Eq. (11).

The damage-coupled elasto-plastic constitutive model and damage evolution model are implemented through the user-defined subroutine called at all material integration points at the beginning of each time increment. The stresses and solution-dependent state variables are updated at the end of each time increment, which is followed by the update of the corresponding Jacobian matrix. [42–47]. Because it is computationally expensive to simulate each loading cycle, the jump-in-cycles procedure is adopted in the numerical implementation, which assumes that the stress, accumulated plastic strain and damage variable remain unchanged in a finite period of ΔN cycles. A simplified flowchart of the numerical algorithm is shown in Fig. 8 and the detailed computational procedures can be referred in the literature [15,16,48].

4. Results and discussion

4.1. Fatigue lifetime results

The fatigue lifetimes of welded joints with different pore conditions are illustrated in Fig. 9 [30]. The vertical axis represents the amplitude of the applied fatigue stress and the horizontal axis is the logarithm scale of number of cycles to cause failure. Pores with the maximum diameter and maximum possession rate occur in the

Table 4
Material parameters of the constitutive model.

E (MPa)	ν	σ_l (MPa)	C_1 (MPa)	γ_1	C_2 (MPa)	γ_2
68000	0.3	327	23777	326.6	76774.7	1940.7

Table 5
Material parameters of the damage evolution model.

<i>a</i>	<i>b</i>	<i>c</i>	β
2.4766e–29	0.0003	0.4406	9.4321

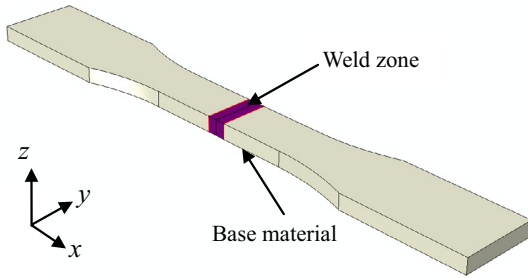


Fig. 7. Model of welded specimen.

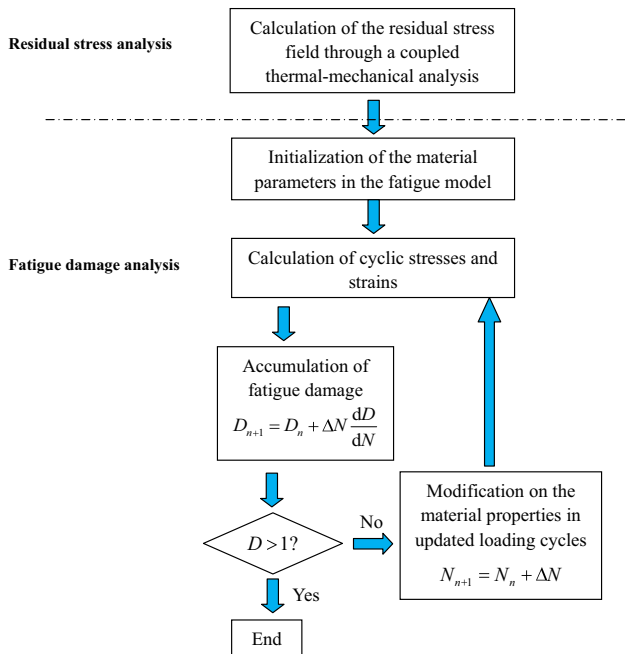


Fig. 8. Flowchart of the numerical simulation.

condition of 70% humidity. It is shown that the fatigue strengths exhibit an inversely proportional relationship with the maximum diameter. The fatigue limit reduces from about 104 MPa to 69 MPa as the maximum diameter increases from 0.06 to 0.72 mm. Through the fracture morphologies analysis of broken joints, the fatigue cracks mainly originate from the largest pore and lead to the final failure. Because both the residual stresses and porosity exist intrinsically in the welded specimens, their combined effects on the fatigue lifetimes are investigated in this study.

The predicted results of fatigue lifetimes are also illustrated by the marked lines in Fig. 9. In the simulation, the obtained residual stress field is assumed to be identical for all specimens under different humidity conditions. The maximum pore diameter listed in Table 3 is used to evaluate the stress concentration. Therefore, the differences of the residual stresses and porosity in specimens under the same humidity level are not considered in this study. Also the scatter of testing results cannot be described through this CDM approach. The maximum deviations between the predicted and testing results occur in the cases near the fatigue limit under

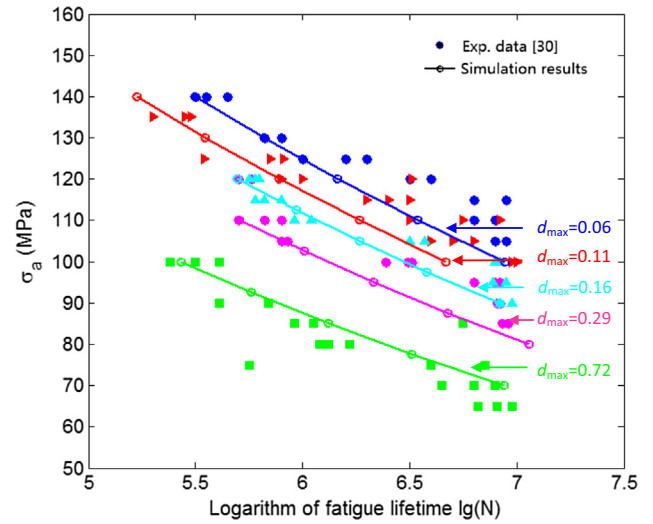


Fig. 9. Testing and prediction results for the fatigue lifetimes of welded joints.

the condition of $d_{max} = 0.06$, which still fall within the three scatter bands. Nevertheless, the predicted results agree well with the testing data.

The stress concentration factors induced by pores are listed in Table 6. Taking the condition of $d_{max} = 0.72$ as an example, the elastic stress concentration factor induced by single pore embedded in bulk materials is around 1.90, which is slightly larger than the result calculated by $1 + d_{max}^c$. It is because that the plastic deformation occurs in the welded zone. Therefore, the reduction of fatigue lifetimes caused by the porosity is significant due to the high stress concentration.

4.2. Evolution of fatigue damage

The simulation under the conditions $\sigma_a = 100$ MPa and $d_{max} = 0.72$ mm is used to describe the evolution of fatigue damage. The damage distribution on the gauge part of the middle cross section is shown in Fig. 10 before the initiation of fatigue crack. The fatigue damage concentrates in the tensile residual stresses zone. The maximum damage close to the critical value 1.0 occurs at the position of the maximum residual stress σ_x due to its same direction as the applied cyclic loading. The evolution of fatigue damage at this point is shown in Fig. 11. In the first half period of whole lifetime, the fatigue damage increases slowly as the number of cycles increases. A linear relationship between the fatigue damage and number of cycles is observed. When the fatigue damage reaches around 0.3, its growth increases significantly, leading to the specimen failure.

The total stress in the weld zone is the superposition of the residual stresses and external cyclic loading. The maximum Mises stress calculated in the first cycle already exceeds the yield stress. The materials in the plastic zone are hardened after the first cycle. Due to the zero stress ratio, no compression plastic deformation can exist. If the fatigue damage is not considered in the constitutive model, plastic strain will no longer occur after the first loading cycle. In this study, the material properties degenerate with the accumulation of fatigue damage and thus the yield function will be satisfied in the subsequent fatigue loading cycles [49]. The accumulation of accumulated plastic strain for the material at the point with maximum damage is also illustrated in Fig. 11, which indicates that the plastic strain exists in each block of ΔN cycles. The increment of the plastic strain in the first cycle is obvious. After the hardening of the materials, the plastic strain is induced by

Table 6
Stress concentration factor induced by pores.

d_{\max} (mm)	0.06	0.11	0.16	0.29	0.72
$1 + d_{\max}^c$	1.2895	1.3781	1.4460	1.5796	1.8652

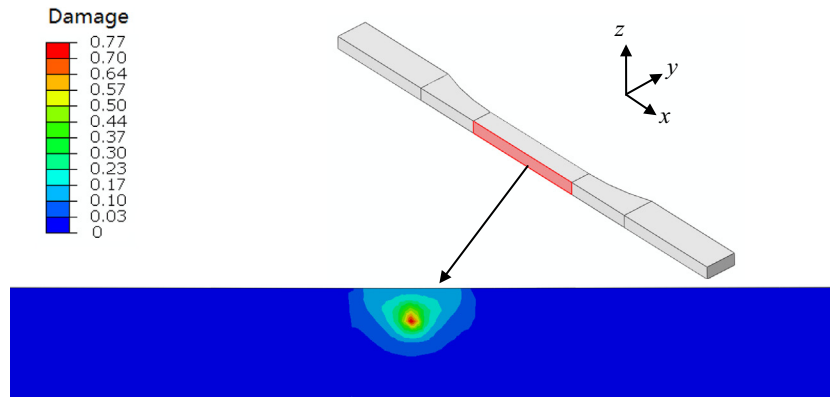


Fig. 10. Damage contour on the gauge part of the middle cross section for $\sigma_a = 100$ MPa, $d_{\max} = 0.72$ mm.

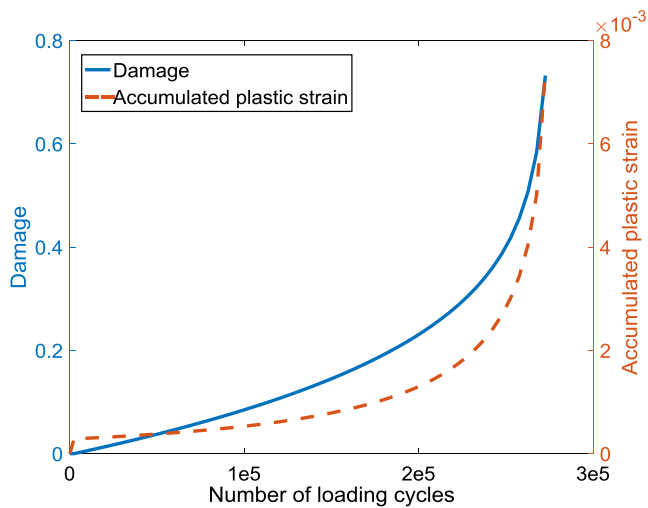


Fig. 11. Evolution of the fatigue damage and accumulated plastic strain at the maximum damage point.

the fatigue damage in the following cycles. Therefore, its evolution with respect to the number of loading cycles is quite similar as that of the fatigue damage, as shown in Fig. 11.

4.3. Residual stress relaxation

The process of residual stress relaxation is also investigated through the prediction under the conditions $\sigma_a = 100$ MPa and $d_{\max} = 0.72$ mm. The relaxation of two components of the residual stresses for the material at the point with maximum damage is illustrated in Fig. 12. A dramatic drop of both components is observed in the first cycle. Especially, the decrease of the component σ_x from about 300 MPa to 248 MPa is more obvious than that of σ_y . It is because the external cyclic stress is applied in the x -direction and thus the plastic strain in this direction is much larger than that in the y -direction. In the loading period of the first cycle, the significant plastic strain leads to the redistribution of the residual stresses due to the obvious plastic strain [50]. After that there is an elastic unloading period until the complete disappearance of the

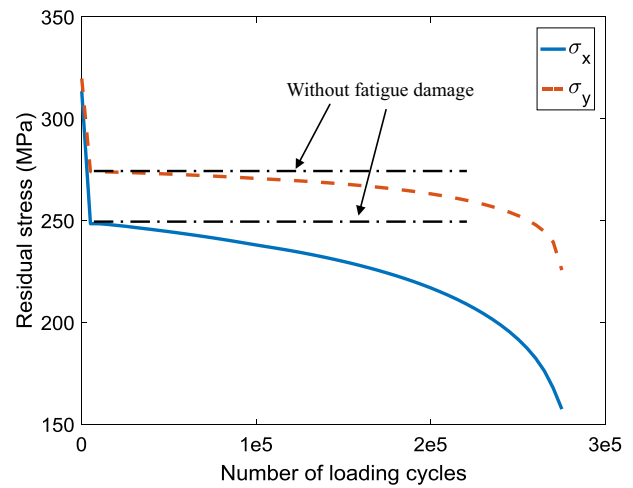


Fig. 12. Residual stress relaxation at the maximum damage point for $\sigma_a = 100$ MPa, $d_{\max} = 0.72$ mm.

external cyclic loading because of the zero stress ratio. In the subsequent cycles, the plastic deformation induced by the fatigue damage still exists as shown in Fig. 11 and therefore the residual stresses decrease gradually. The speed of the residual stress relaxation increases as the fatigue damage increases, especially for the stress σ_x . If the fatigue damage is not incorporated into the constitutive model, the elastic shakedown will be observed and the residual stresses will remain a stabilized state after the first cycle, as the dash-dot line shown in Fig. 12. It is indicated that the relaxation of the residual stresses is the combined effects of the plastic deformation and fatigue damage.

5. Conclusions

This study investigated the fatigue damage evolution of welded joints under cyclic loading with the consideration of residual stresses and porosity in a CDM approach. A coupled thermo-mechanical analysis was used to evaluate the residual stresses in the welded specimens. The multiaxial tensile residual stresses concentrate in the weld zone and the maximum value is close to the

material yield stress. The residual stress field is then used as the initial state of the fatigue damage analysis. A fatigue damage model that considers the elasto-plastic deformation and stress concentration induced by the pores are employed to predict the fatigue lifetimes of joints with different pore conditions.

The proposed CDM approach can provide reasonable predictions of fatigue lifetimes for welded joints with detectable pores induced in the welding processes. It is also indicated that the weld-induced residual stresses should be taken into account in the fatigue damage analysis. Due to the material damage, the elastic shakedown after the plastic deformation in the first cycle is not observed and the plastic strain exists in the successive cycles. A dramatic relaxation of the residual stresses occurs in the first cycle due to the large plastic deformation. In the subsequent cycles, the residual stresses also gradually decrease due to the fatigue damage. Therefore, the relaxation of the residual stresses is attributed to the combined effects of the plastic deformation and fatigue damage.

Acknowledgments

The authors acknowledge the financial support from Singapore Maritime Institute (Grant No: SMI-2014-MA11).

References

- [1] Radaj D, Sonsino CM, Fricke W. *Fatigue assessment of welded joints by local approaches*. Cambridge: Woodhead Publishing; 2006.
- [2] Fricke W. *Fatigue analysis of welded joints: state of development*. *Mar Struct* 2003;16(3):185–200.
- [3] Eurocode 9. *Design of aluminum structures: Part 2: structures susceptible to fatigue*. Brussels: CEN; 1998 [ENV, 1999-2].
- [4] International Institute of Welding. *Fatigue design of welded joints and components*. Cambridge: Abington Publishing; 1996.
- [5] Buffière JY, Savelli S, Jouneau PH, et al. Experimental study of porosity and its relation to fatigue mechanisms of model Al–Si₇–Mg_{0.3} cast Al alloys. *Mater Sci Eng A – Struct* 2001;316(1):115–26.
- [6] Mayer H, Papakyriacou M, Zettl B, Stanzl-Tschegg SE. Influence of porosity on the fatigue limit of die cast magnesium and aluminium alloys. *Int J Fatigue* 2003;25(3):245–56.
- [7] Do DK, Li P. The effect of laser energy input on the microstructure, physical and mechanical properties of Ti-6Al-4V alloys by selective laser melting. *Virtual Phys Prototyp* 2016;11(1):41–7.
- [8] Panchagnula JS, Simhambhatla S. Inclined slicing and weld-deposition for additive manufacturing of metallic objects with large overhangs using higher order kinematics. *Virtual Phys Prototyp* 2016;11(2):99–108.
- [9] Madison JD, Aagesen LK. Quantitative characterization of porosity in laser welds of stainless steel. *Scripta Mater* 2012;67:783–6.
- [10] Zhang C, Gao M, Wang DZ, Yin J, Zeng XY. Relationship between pool characteristic and weld porosity in laser arc hybrid welding of AA6082 aluminum alloy. *J Mater Process Technol* 2017;240:217–22.
- [11] Dinda SK, Warnett JM, Williams MA, Roy GG, Srirangam P. 3D imaging and quantification of porosity in electron beam welded dissimilar steel to Fe-Al alloy joints by X-ray tomography. *Mater Design* 2016;96:224–31.
- [12] Fricke W. *Fatigue strength assessment of local stresses in welding joints*. In: MacDonald KA, editor. *Fracture and fatigue of welded joints and structures*. Oxford: Woodhead Publishing; 2011. p. 115–38.
- [13] Hobbacher A. The use of fracture mechanics in the fatigue analysis of welded joints. In: MacDonald KA, editor. *Fracture and fatigue of welded joints and structures*. Oxford: Woodhead Publishing; 2011. p. 91–112.
- [14] Maddox SJ. Review of fatigue assessment procedures for welded aluminum structures. *Int J Fatigue* 2003;25:1359–78.
- [15] Shen F, Hu WP, Meng QC. A non-local approach based on the hypothesis of damage dissipation potential equivalence to the effect of stress gradient in fretting fatigue. *Int J Fatigue* 2016;90:125–38.
- [16] Shen F, Hu WP, Vuyiadjis GZ, Meng QC. Effects of fatigue damage and wear on fretting fatigue under partial slip condition. *Wear* 2015;338:394–405.
- [17] Do VNV, Lee CH, Chang KH. High cycle fatigue analysis in presence of residual stresses by using a continuum damage mechanics model. *Int J Fatigue* 2015;70:51–62.
- [18] He C, Huang CX, Liu YJ, Wang QY. Fatigue damage evaluation of low-alloy steel welded joints in fusion zone and heat affected zone based on frequency response changes in gigacycle fatigue. *Int J Fatigue* 2014;61:297–303.
- [19] Lemaitre J, Rodrigue D. *Engineering damage mechanics*. New York: Springer; 2005.
- [20] Chaboche JL. Constitutive equations for cyclic plasticity and cyclic viscoplasticity. *Int J Plast* 1989;5:247–302.
- [21] Kang GZ, Liu YJ, Ding J, Gao Q. Uniaxial ratcheting and fatigue failure of tempered 42CrMo steel: damage evolution and damage-coupled visco-plastic constitutive model. *Int J Plast* 2009;25(5):838–60.
- [22] Xiao YC, Li S, Gao Z. A continuum damage mechanics model for high cycle fatigue. *Int J Fatigue* 1998;20(7):503–8.
- [23] Chaudonneret M. A simple and efficient multiaxial fatigue damage model for engineering applications of macro-crack initiation. *J Eng Mater – Trans ASME* 1993;115(4):373–9.
- [24] Shen F, Hu WP, Meng QC, Zhang M. A new damage mechanics based approach to fatigue life prediction and its engineering application. *Acta Mech Solida Sin* 2015;28(5):510–20.
- [25] Chan KS. Roles of microstructure in fatigue crack initiation. *Int J Fatigue* 2010;32(9):1428–47.
- [26] Sadeghi F, Jalalahmadi B, Slack TS, Raje N, Arakere NK. A review of rolling contact fatigue. *J Tribol – Trans ASME* 2009;131(4):041403.
- [27] Fan J, McDowell DL, Horstemeyer MF, Gall K. Cyclic plasticity at pores and inclusions in cast Al–Si alloys. *Eng Fract Mech* 2003;70(10):1281–302.
- [28] Prasannavenkatesan R, Przybyla CP, Salajegheh N, McDowell DL. Simulated extreme value fatigue sensitivity to inclusions and pores in martensitic gear steels. *Eng Fract Mech* 2011;78(6):1140–55.
- [29] Naderi M, Hoseini SH, Khonsari MM. Probabilistic simulation of fatigue damage and life scatter of metallic components. *Int J Plast* 2013;43:101–15.
- [30] Gou G, Zhang M, Chen H, Chen J, Li P, Yang YP. Effect of humidity on porosity, microstructure, and fatigue strength of A7N015-T5 aluminum alloy welded joints in high-speed trains. *Mater Design* 2015;85:309–17.
- [31] Bouafia F, Boualem S, El Amin MM, Benali B. 3-D finite element analysis of stress concentration factor in spot-welded joints of steel: the effect of process-induced porosity. *Comput Mater Sci* 2011;50(4):1450–9.
- [32] Zhu Q, Chen J, Gou G, Chen H, Li P. Ameliorated longitudinal critically refracted–attenuation velocity method for welding residual stress measurement. *J Mater Process Technol* 2017;246:267–75.
- [33] Goldak J, Chakravarti A, Bibby M. A new finite element model for welding heat sources. *Metall Mater Trans B* 1984;15(2):299–305.
- [34] Price JWH, Ziara-Paradowska A, Joshi S, Finlayson T, Semetay C, Nied H. Comparison of experimental and theoretical residual stresses in welds: the issue of gauge volume. *Int J Mech Sci* 2008;50(3):513–21.
- [35] Yan DJ, Liu XS, Li J, Yang JG, Fang HY. Effect of strain hardening and strain softening on welding distortion and residual stress of A7N01-T4 aluminum alloy by simulation analysis. *J Cent South Univ Technol* 2010;17:666–73.
- [36] Deng D, Murakawa H. Numerical simulation of temperature field and residual stress in multi-pass welds in stainless steel pipe and comparison with experimental measurements. *Comput Mater Sci* 2006;37(3):269–77.
- [37] Lopez-Jauregi A, Ulacia I, Esnaola JA, Ugarte D, Torca I. Procedure to predict residual stress pattern in spray transfer multipass welding. *Int J Adv Manuf Technol* 2015;76(9–12):2117–29.
- [38] Liang W, Murakawa H, Deng D. Investigation of welding residual stress distribution in a thick-plate joint with an emphasis on the features near weld end-start. *Mater Design* 2015;67:303–12.
- [39] Xia J, Jin H. Numerical study of welding simulation and residual stress on butt welding of dissimilar thickness of austenitic stainless steel. *Int J Adv Manuf Technol* 2016:1–9.
- [40] Elmeslamy A, Francis JA, Li L. A comparison of residual stresses in multi pass narrow gap laser welds and gas-tungsten arc welds in AISI 316L stainless steel. *Int J Press Ves Pip* 2014;113:49–59.
- [41] Kaufman JG. *Properties of aluminum alloys: fatigue data and the effects of temperature, product form, and processing*. ASM International; 2008.
- [42] Simo JC, Taylor RL. Consistent tangent operator for rate-independent elastoplasticity. *Comput Method Appl Mech* 1985;48:101–18.
- [43] Kang GZ. Finite element implementation of visco-plastic constitutive model with strain-range-dependent cyclic hardening. *Int J Numer Methods Biomed Eng* 2006;22(2):137–53.
- [44] Kan QH, Kang GZ, Zhang J. Uniaxial time-dependent ratchetting: visco-plastic model and finite element application. *Theor Appl Fract Mech* 2007;47(2):133–44.
- [45] Kang GZ. A visco-plastic constitutive model for ratchetting of cyclically stable materials and its finite element implementation. *Mech Mater* 2004;36:299–312.
- [46] Kang GZ. Ratchetting: recent progresses in phenomenon observation, constitutive modeling and application. *Int J Fatigue* 2008;30:1448–72.
- [47] Belytschko T, Liu WK, Moran B. *Nonlinear finite elements for continua and structures*. Chichester: Wiley; 2000.
- [48] Sun Y, Hu WP, Shen F, Meng QC, Xu YM. Numerical simulations of the fatigue damage evolution at a fastener hole treated by cold expansion or with interference fit pin. *Int J Mech Sci* 2016;107:188–200.
- [49] Pham TH, Kim SE. Microstructure evolution and mechanical properties changes in the weld zone of a structural steel during low-cycle fatigue studied using instrumented indentation testing. *Int J Mech Sci* 2016;114:141–56.
- [50] Laamouri A, Sidhom H, Braham C. Evaluation of residual stress relaxation and its effect on fatigue strength of AISI 316L stainless steel ground surfaces: experimental and numerical approaches. *Int J Fatigue* 2013;48:109–21.